

CHIMPS2: The physical properties and star formation efficiency of molecular gas in the Central Molecular Zone

S. M. King¹*, T. J. T. Moore¹, S. N. Longmore¹, D. J. Eden^{2,3}, J. D. Henshaw⁴, A. J. Rigby⁵, R. Rani⁶

¹ Astrophysics Research Institute, Liverpool John Moores University, IC2, Liverpool Science Park, 146 Brownlow Hill, Liverpool, L3 5RF, UK

² Department of Physics, University of Bath, Claverton Down, Bath, BA2 7AY, UK

³ Armagh Observatory and Planetarium, College Hill, Armagh, BT61 9DB, UK

⁴ Max-Planck-Institut für Astronomie, Königstuhl 17, 69117 Heidelberg, Germany

⁵ School of Physics and Astronomy, University of Leeds, Leeds, LS2 9JT, UK

⁶ Institute of Astronomy, National Tsing Hua University, General Building II No. 101, Sec. 2, Kuang-Fu Road, Hsinchu 30013, Taiwan, R.O.C.

Accepted XXX. Received YYY; in original form ZZZ

ABSTRACT

We present Local Thermodynamic Equilibrium (LTE) estimates of the physical properties and star formation efficiency (SFE) of molecular gas in the Central Molecular Zone (CMZ), using new ^{12}CO $J = 2 \rightarrow 1$ observations from the James Clerk Maxwell Telescope. Combined with CHIMPS2 ^{12}CO and ^{13}CO $J = 3 \rightarrow 2$, and SEDIGISM ^{13}CO $J = 2 \rightarrow 1$ data, we estimate a median excitation temperature of $T_{\text{ex}} = 11$ K for ^{13}CO throughout the CMZ, with peaks exceeding 120 K in the Sgr B1/B2 complex. Cooler gas dominates around Sgr A and nearby clouds. We derive a median H_2 column-density of $N(\text{H}_2) = 2 \times 10^{22} \text{ cm}^{-2}$ and a total ^{13}CO -traced gas mass of $M_{\text{gas}} = 7 \times 10^6 \text{ M}_\odot$, consistent with previous estimates when accounting for spatial coverage. The instantaneous SFE is assessed using Hi-GAL compact sources detected at 70- μm and 160–500- μm . The 70- μm -bright SFE, tracing current star formation, is modest overall but elevated in Sgr B1/B2, the Arches cluster, and Sgr C. In contrast, the 160–500- μm SFE, tracing cold pre-stellar gas, is more broadly enhanced, particularly in the dust ridge clouds and towards negative longitudes surrounding Sgr C. The contrasting distributions suggest an evolutionary gradient in SFE, consistent with a transition from dense, cold gas to embedded protostars. Our results imply that the CMZ may be enter a more active phase of star formation, with large reservoirs of gas primed for future activity.

Key words: ISM: molecules — ISM: structure — submillimetre: ISM — stars: formation — Galaxy: centre

1 INTRODUCTION

Star formation is one of the most important processes that drive galaxy evolution, enriching the interstellar medium (ISM) with metals and continually altering the balance between gas and stars within galaxies. Understanding the conditions and processes that govern star formation is crucial for explaining the evolutionary pathways of galaxies and for developing a predictive model of star formation. At present, it is not known how the star formation process is impacted by the physical conditions present in the local ISM.

The Central Molecular Zone (CMZ), the inner 500 parsecs of our Galaxy, contains approximately 5 per cent of the Milky Way's total molecular gas, estimated to be on the order of 10^7 M_\odot (Dahmen et al. 1998; Oka et al. 1998; Nakanishi & Sofue 2006; Henshaw et al. 2023). Despite its relatively small contribution to the total molecular gas budget, the CMZ hosts some of the most extreme environments for star formation in the Galaxy. Moreover, the CMZ contains a disproportionately large fraction of the denser, star-forming gas. Approximately 80 per cent of the Milky Way's molecular gas at high densities, in which gravitational collapse is most likely to lead to

star formation, is found here (Morris & Serabyn 1996; Ferrière et al. 2007; Longmore et al. 2013).

Yet despite this abundance of dense molecular gas, the star formation rate per unit of dense gas in the CMZ is estimated to be an order of magnitude lower than in the spiral arms (cf. Lada et al. 2012; Longmore et al. 2013), and understanding why the star formation efficiency (SFE) is so low in the CMZ, despite its high gas density, is a significant challenge (Kruissel et al. 2014; Rathborne et al. 2014; Barnes et al. 2017a; Dale et al. 2019).

Dense-gas temperatures derived from the observations of molecules such as metastable ammonia (NH_3) and para-formaldehyde (p- H_2CO) in the Galactic centre range from approximately 60 K to over 100 K in several regions, while highest gas temperatures are observed around Sgr B2, the 20- km s^{-1} and 50- km s^{-1} clouds, and in The Brick (Ginsburg et al. 2016; Krieger et al. 2017).

These elevated temperatures suggest that the internal thermal energy of gas in the CMZ is higher compared to molecular clouds in the spiral arms. However, the broad line widths observed in dense gas within the central ~ 250 pc of the Galaxy are mostly due to turbulent motions rather than thermal broadening. Line widths here range between 5 and 10 km s^{-1} on parsec scales (Henshaw et al. 2016b) and between 8 and 16 km s^{-1} on scales of individual molecular clouds (~ 10 to

* E-mail: arisking@ljmu.ac.uk (SMK)

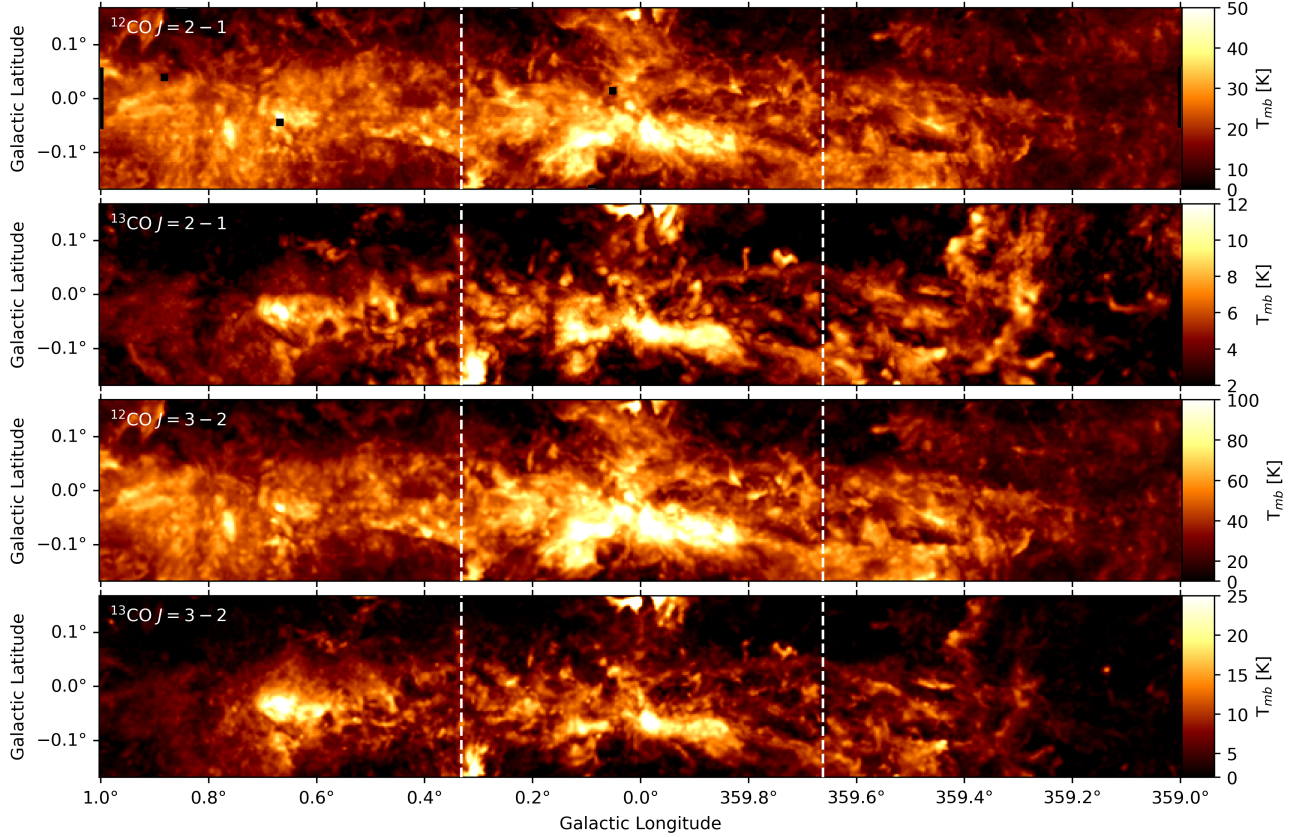


Figure 1. The peak main-beam temperature maps of the CMZ before smoothing for the transitions and isotopologues of CO. **Top:** $^{12}\text{CO } J = 2 \rightarrow 1$ (this work). The masked pixels (NaN values) are those with $\text{SNR} < 5$. **Second:** $^{13}\text{CO } J = 2 \rightarrow 1$ (Schuller et al. 2017). **Third:** $^{12}\text{CO } J = 3 \rightarrow 2$ (Eden et al. 2020). **Bottom:** $^{13}\text{CO } J = 3 \rightarrow 2$ (King et al. 2024). The top, third, and bottom maps were smoothed for the analysis to match the resolution of the second panel. The white dashed lines divide the regions containing one of the Sagittarius complexes (Sgr B, Sgr A, and Sgr C from left to right).

50 pc) (Krieger et al. 2017). Conversely, typical line widths of disc clouds are 3–5 times smaller than in the CMZ. Typically, line widths here are $1 - 10 \text{ km s}^{-1}$ (Mills 2017). Analysis of molecular clouds and clumps in the Galactic Ring Survey (GRS) (Jackson et al. 2006) also found that the typical line widths of molecular clouds in the Galactic plane are significantly narrower, often less than 10 km s^{-1} (Rathborne et al. 2009).

Previous studies, such as the investigation by Eden et al. (2015), matched infrared-selected young stellar objects (YSOs) with dense molecular clumps across different Galactic environments to assess the SFE. Their findings demonstrated that the SFE, measured as the mean infrared luminosity-to-mass ratio ($L_{\text{IR}}/M_{\text{clump}}$), is slightly enhanced in spiral arms compared to interarm regions on kiloparsec scales.

However, they also found that intrinsic variations within individual clumps dominate the overall range of SFE, with $L_{\text{IR}}/M_{\text{clump}}$ spanning three orders of magnitude and following a log-normal distribution. Additionally, a strong linear correlation was observed between L_{IR} and M_{clump} , indicating that star formation activity scales directly with dense gas mass, independent of Galactic location. Our study builds on these findings by investigating whether similar trends and variations in SFE are observed in the CMZ, a unique Galactic environment characterized by extreme gas densities and turbulent conditions.

In a previous study (King et al. 2024), we presented the initial data for the $J = 3 \rightarrow 2$ transition of ^{13}CO obtained from the CMZ

as part of the CO Heterodyne Inner Milky Way Plane Survey 2 (CHIMPS2) (Eden et al. 2020). Covering $358.8 \leq \ell \leq 1.2$ and $|b| \leq 0.5$, our observations unveiled the complex structure of the molecular gas of the CMZ in improved detail. We estimated ^{13}CO and H_2 column densities using simplified assumptions about temperature and explored the relationship between the integrated intensity of ^{13}CO and the surface density of compact infrared sources identified by *Herschel* Hi-GAL (Molinari et al. 2011; Molinari et al. 2016; Elia et al. 2017).

Building on this foundation, this paper presents a more in-depth analysis of the excitation conditions within the CMZ to extract accurate key physical properties such as excitation temperature, column density, and ^{13}CO -traced gas mass. We use the same ^{12}CO and $^{13}\text{CO } J = 3 \rightarrow 2$ data as previously (Eden et al. 2020; King et al. 2024), accompanied by $^{13}\text{CO } J = 2 \rightarrow 1$ from the SEDIGISM survey (Schuller et al. 2017). We also present new $^{12}\text{CO } J = 2 \rightarrow 1$ observations from the JCMT, which complete the isotopologue ladder for these transitions in the CMZ, allowing us to trace these properties by conducting a full excitation analysis under the assumption of Local Thermodynamic Equilibrium (LTE). We expand on previous studies by presenting column-density estimates using these derived excitation temperatures and total ^{13}CO -traced gas mass estimates.

Lastly, we investigate the instantaneous star formation efficiency (SFE) of the CMZ using the ratio of the integrated bolometric luminosity of Hi-GAL sources (Molinari et al. 2016; Elia et al. 2017; Elia et al. 2021) to gas mass. Section 2 details the data sets and pro-

cessing methods used, Section 3 discusses the LTE analysis of the data, Section 4 examines the star formation efficiency of the CMZ, and Section 5 summarises the findings of the article.

2 DATA

2.1 The CHIMPS2 Survey

The CHIMPS2 observations were carried out using the 15-m James Clark Maxwell Telescope (JCMT) in Hawaii, which has a diffraction-limited angular resolution of 15 arcsec at 330.587 GHz. The Heterodyne Array Receiver Program (HARP) was used in conjunction with the Auto-Correlation Spectral Imaging System (ACIS) backend (Buckle et al. 2009) to observe ^{12}CO and ^{13}CO in the CMZ with a binned channel width of 1 km s^{-1} . The CMZ portion of the CHIMPS2 survey employed a systematic observing strategy, as outlined in Eden et al. (2020), between Galactic longitudes $357^\circ \leq \ell \leq 5^\circ$ and latitudes $|b| \leq 0.5^\circ$ in ^{12}CO , and $358.8^\circ \leq \ell \leq 1.4^\circ, |b| \leq 0.5^\circ$ in ^{13}CO . The spectral cubes have native angular resolutions of 14 arcsec for ^{12}CO and 15 arcsec for ^{13}CO . These were convolved with Gaussian beams of 9 arcsec and 8 arcsec, respectively, resulting in a final angular resolution of 17 arcsec. The data have a spectral resolution of 1 km s^{-1} and an rms noise level in T_A^* of 0.58 K for ^{12}CO and 0.59 K for ^{13}CO , using 6 arcsec pixels.

2.2 The SEDIGISM Survey

The SEDIGISM survey covers 78 square degrees of the inner Galaxy ($-60^\circ \leq \ell \leq 18^\circ, |b| \leq 0.5^\circ$) in the $J = 2 \rightarrow 1$ rotational transition of ^{13}CO . The SEDIGISM data achieved a spatial resolution of 30 arcseconds and a velocity resolution of 0.25 km s^{-1} (Schuller et al. 2017). The survey achieved mean rms sensitivities of $\sigma(T_{\text{mb}}) \approx 0.8 \text{ K}$ per 0.25-km s^{-1} velocity channel for ^{13}CO , although the sensitivity varies across the survey region due to differing weather conditions. The main-beam efficiency of the APEX telescope used in the ^{13}CO $J = 2 \rightarrow 1$ SEDIGISM data is $\eta_{\text{mb}} = 0.73$ (Güsten et al. 2006).

2.3 Complementary JCMT Observations

This paper also presents additional observations that complement the survey data sets, conducted using 'U', one of the three receiver inserts within the Nāmakanui instrument on the JCMT (Mizuno et al. 2020). These data cover the $J = 2 \rightarrow 1$ rotational transition of ^{12}CO at 230.538 GHz within Galactic longitudes $359^\circ \leq \ell \leq 1^\circ$ and latitudes $|b| \leq 0.1^\circ$, as shown in the top panel of Fig. 1. The observations have a native angular resolution of 24 arcsec at 230.538 GHz, with a spectral resolution of 1 km s^{-1} , and achieve an rms sensitivity of 1 K per 0.25-km s^{-1} channel on 10 arcsec pixels.

2.4 Data Calibration and Resolution Matching

For consistency in resolution, the CHIMPS2 data were first smoothed using the Starlink KAPPA routine GAUSMOOTH (Currie et al. 2014) to match the SEDIGISM spatial resolution of 30 arcsec. The datasets were then converted from the corrected antenna-temperature scale (T_A^*) to the main-beam brightness temperature scale (T_{mb}) using:

$$T_{\text{mb}} = \frac{T_A^*}{\eta_{\text{mb}}}. \quad (1)$$

For this conversion, main-beam efficiencies of $\eta_{\text{mb}} = 0.605$ and 0.72

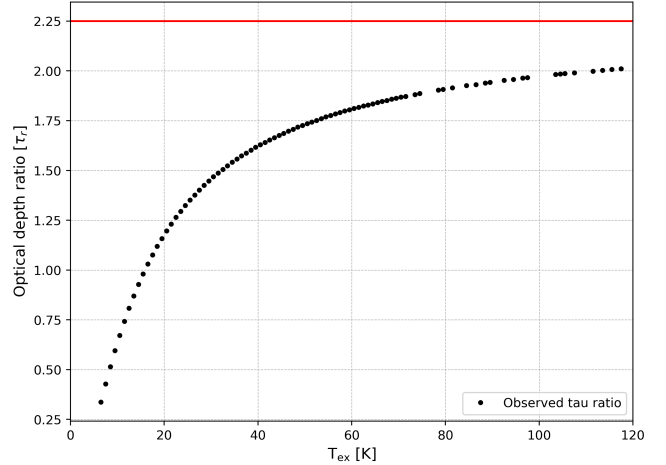


Figure 2. The $J = 3 \rightarrow 2/J = 2 \rightarrow 1$ optical-depth ratio of ^{13}CO as a function of excitation temperature (T_{ex}) of ^{13}CO determined using Equation 3. The red line represents the high-temperature limit at $\tau_r = 2.25$, above which no solution is found.

were adopted for the CHIMPS2 $J = 3 \rightarrow 2$ ^{12}CO and ^{13}CO data, respectively (Buckle et al. 2009).

Similarly, the JCMT ^{12}CO $J = 2 \rightarrow 1$ observations were binned into 1-km s^{-1} channels and smoothed to achieve a final angular resolution of 30 arcsec, matching the SEDIGISM and CHIMPS2 datasets. The resulting rms sensitivity of the smoothed new data is 0.46 K per 1-km s^{-1} channel. The main-beam efficiency adopted for these data is $\eta_{\text{mb}} = 0.57$ (Mizuno et al. 2020).

These processed datasets enable full LTE derivations of excitation conditions and physical parameters of CO-traced gas in the CMZ in the region covered by the JCMT ^{12}CO $J = 2 \rightarrow 1$ observations where all four transitions are available. To ensure the reliability of extracted signals, all datasets were masked to remove emission with a signal-to-noise ratio (SNR) < 3 , corresponding to a 3σ threshold. The data quality was assessed by calculating the fraction of sight lines with emission above 3σ significance. Both the ^{12}CO and ^{13}CO transitions show nearly complete detection across the entire mapped region, with 100% of sight lines exceeding 3σ significance in the $J = 3 \rightarrow 2$ transitions and 99.95% in the $J = 2 \rightarrow 1$ transitions.

Finally, both the CHIMPS2 and SEDIGISM datasets were trimmed using wcsalign to match the coverage and pixel grid of the new JCMT observations. The final rms sensitivities for these smoothed datasets are 0.2 K for CHIMPS2 $J = 3 \rightarrow 2$ ^{12}CO and 0.1 K for ^{13}CO , both lower than those reported in (Eden et al. 2020) and (King et al. 2024). The trimmed and smoothed SEDIGISM $J = 2 \rightarrow 1$ ^{13}CO data reached an rms sensitivity of 0.2 K.

3 PHYSICAL PROPERTIES OF THE CMZ

In this section, we present estimates of the physical properties of the CMZ determined using ^{13}CO under the assumption of local thermodynamic equilibrium (LTE). We assume that the brightness temperatures (T_B) match the measured main-beam temperatures (T_{mb}). Fig. 1 compares the peak main-beam temperatures for the transitions and isotopologues of CO used in this paper. The integrated-intensity maps were presented King et al. (2024); however, in this work, we focus on peak-intensity maps to emphasize the maximum observed values, and to highlight regions with potentially higher excitation

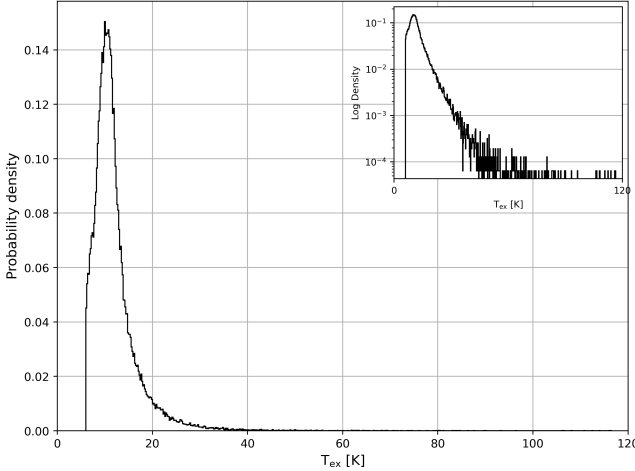


Figure 3. Histogram of the distribution of ^{13}CO excitation temperature (T_{ex}) values, calculated from the data under the assumption of Local Thermodynamic Equilibrium (LTE). The median T_{ex} is 11^{+2}_{-2} K. The excitation temperature values were determined using the method described in Section 3.2. The inset plot shows the same distribution on a log-y scale.

conditions. This also mitigates the impact of the very broad lines observed in the CMZ.

3.1 Optical depth ratio

3.1.1 Observed Ratio Calculation

The ^{13}CO optical depth of both transitions arises from the solution to the equation of radiative transfer, and was calculated using the ratio of ^{13}CO to ^{12}CO T_{mb} for each transition, by assuming that the ^{12}CO optical depth (τ_{12}) is much greater than 1, as follows:

$$\tau_{13} = -\ln(1 - (T_{\text{mb},13}/T_{\text{mb},12})) \quad (2)$$

Assuming Local Thermodynamic Equilibrium (LTE) and a single excitation temperature along the line of sight, the optical depth ratio of two adjacent transitions of the same isotopologue is derived from detailed balance, under the assumption that the population levels are described by a Boltzmann distribution, such that, for $J = 3 - 2$ and $J = 2 - 1$:

$$\tau_r = \frac{\tau(3, 2)}{\tau(2, 1)} = \left(\frac{3}{2}\right) \left(\frac{1 - \exp\left(-\frac{6hB}{kT_{\text{ex}}}\right)}{\exp\left(\frac{4hB}{kT_{\text{ex}}}\right) - 1} \right) \quad (3)$$

Where B is the ^{13}CO rotation constant in frequency units ($B = 55.10$ GHz), defined by $B = h/8\pi^2 I$, I is the moment of inertia and h is the Planck constant.

3.2 Excitation Temperature Determination Using a Look-Up Table Method

The ^{13}CO excitation temperature (T_{ex}) was determined using a computational look-up table approach based on Equation 3. A theoretical look-up table of 87,362 optical depth ratios (τ_r) was generated for

excitation temperatures spanning 0–200 K, this number of grid points was chosen to match the total number of pixels in the 2D maps providing a direct mapping between each ratio and its corresponding T_{ex} .

For each pixel, the ^{13}CO optical depths for the $J = 3 \rightarrow 2$ and $J = 2 \rightarrow 1$ transitions were computed using Equation 2. The ratio of these optical depths was then compared to the theoretical values in the look-up table (as in Fig. 2) to find the closest match. The associated T_{ex} with the closest matching theoretical τ_r value was then assigned to that pixel to produce the distributions shown in Fig. 3 and Fig. 4.

LTE limitations: Equation 2 will fail when $T_{\text{mb},13} \geq T_{\text{mb},12}$, or when $T_{\text{mb},12} = 0$, although the latter is not realistic given the 3σ threshold, we include it here for completeness. Typically, $T_{\text{mb},13}$ is lower than $T_{\text{mb},12}$, however, in regions with strong gradients in temperature along the line of sight, or in the presence of self-absorption, the assumption of a single excitation temperature can become inaccurate due to variations in optical depth allowing $T_{\text{mb},13}$ to approach or exceed $T_{\text{mb},12}$.

In regions of high optical depth, this can lead to systematic biases in the derived τ -ratio. Since ^{12}CO is typically more optically thick than ^{13}CO , its emission will be dominated by foreground layers, while ^{13}CO can trace deeper, potentially cooler gas. These effects are more likely to occur in regions better traced by ^{13}CO , specifically where strong emission is observed in both transitions and where high optical depths or ^{12}CO self-absorption are more prevalent. Furthermore, when $\tau_{13,2-1}$ is small and $\tau_{13,3-2} \approx 0$, Equation 3 will also be invalid. This typically occurs in regions where ^{13}CO is not sufficiently detected, which again is unlikely in this case given the 3σ threshold, and is included here only for completeness.

An additional limitation arises from the maximum allowable τ -ratio under the assumption of LTE and a constant T_{ex} along the line of sight. Under these conditions, the ratio τ_r is capped at a theoretical maximum of 9/4 shown as the red line in Fig. 2. This arises because the bracketed exponential term in Equation 3 approaches 3/2 for $T_{\text{ex}} \gg hB/k$, causing the equation to simplify to the general form $\tau_r = (J+1)/J^2$ (where $J = 2$ is the common rotational level). The limit is a direct consequence of the Boltzmann distribution, which governs the population of energy levels in thermal equilibrium.

The assumption of LTE also imposes limitations. The transitions used in this analysis have different critical densities, with the $J = 3 \rightarrow 2$ transition requiring higher densities for thermalisation than $J = 2 \rightarrow 1$. If the gas is sub-thermally excited, particularly for the higher transition, collisional excitation will be inefficient and the observed T_{mb} will be lower than expected under LTE assumptions. This would lead to a systematic underestimation of T_{ex} .

The LTE assumption and the transitions used in this work also suggest a lower cut off of 5.5 K for the derived excitation temperatures, being approximately the excitation energy of the $J = 1$ level of CO. At this temperature, almost all molecules are in either the $J = 1$ or $J = 0$ levels and the $(J = 3 \rightarrow 2)/(J = 2 \rightarrow 1)$ line ratio becomes an unreliable thermometer. The system also enters a regime where the excitation temperature converges to values close to that of the Cosmic Microwave Background (2.73 K), causing the ratio to lose its diagnostic power and become dominated by uncertainties.

Lastly, noise-affected pixels can return unreliable results, particularly in low-intensity regions where fluctuations in $T_{\text{mb},12}$ and $T_{\text{mb},13}$ may be comparable to the signal itself. Nevertheless, deriving the excitation temperature from optical-depth ratios remains a robust and physically well-motivated method.

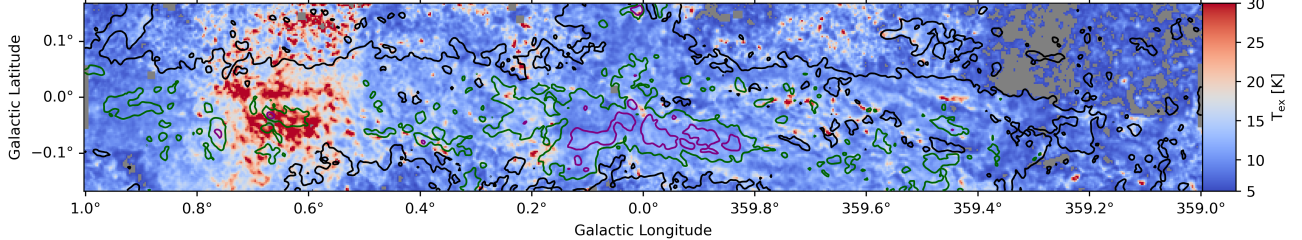


Figure 4. The distribution of the excitation temperature (T_{ex}) across the Central Molecular Zone (CMZ), derived as in Section 3.2. The distribution reaches its peak towards Sgr B, and is similar to the Hi-GAL dust temperature map shown in Molinari et al. (2011). The contour shows the ^{12}CO $J = 3 \rightarrow 2$ peak intensity from Fig. 1 at 30 K (black), 60 K (green) and 90 K (purple). Grey pixels represent regions where $\tau_r > 2.25$, thus no valid solution to Equation 3 is found.

3.3 Column Density and Total gas mass estimates

With an estimate of the ^{13}CO excitation temperature, and assuming the high-temperature approximation for the partition function $Z \approx kT_{\text{ex}}/hB$, we can then determine the column density of ^{13}CO using the following equation:

$$N(^{13}\text{CO}) = \frac{8\pi}{7c^2} \frac{kT_{\text{ex}}}{hB} \frac{\nu_{32}^2}{A_{32}} e^{\frac{6hB}{kT_{\text{ex}}}} \left(1 - e^{-\frac{h\nu_{32}}{kT_{\text{ex}}}}\right)^{-1} \int \tau_{13} d\nu \quad \text{cm}^{-2} \quad (4)$$

Where T_{ex} is the excitation temperature of ^{13}CO , which is assumed to be the same for both the $J = 3 \rightarrow 2$ and $J = 2 \rightarrow 1$ transitions (i.e., both transitions are thermalised), determined in Section 3.2. ν_{32} and $\tau(\nu)$ are the transition frequency and the ^{13}CO optical depth of the 3–2 line, respectively. The integration is performed over all velocity channels between $\nu = \pm 200 \text{ km s}^{-1}$, assuming that the excitation temperature remains uniform across all velocity components, meaning no line-of-sight temperature gradients are present.

We then used the ^{13}CO column density to estimate the H_2 column-density, $N(\text{H}_2)$ assuming an appropriate abundance ratio for ^{13}CO to H_2 , $^{13}\text{CO}/\text{H}_2$ (see subsection 3.4.2). The H_2 column density is therefore:

$$N(\text{H}_2) = \frac{N(^{13}\text{CO})}{[^{13}\text{CO}/\text{H}_2]} \quad (5)$$

When summed over the observed area, $N(\text{H}_2)$ gives the total mass of gas traced by ^{13}CO , in a similar manner to that described in appendix A of Kauffmann et al. (2008), given by:

$$M_{\text{tot}} = \mu_{\text{H}_2} m_{\text{H}} A_{\text{proj}} \sum N(\text{H}_2) \quad (6)$$

where $\mu_{\text{H}_2} \approx 2.72$ is the mean molecular weight per H_2 molecule, accounting for a helium fraction of 0.25, m_{H} is the atomic hydrogen mass in kg, and A_{proj} is the physical area subtended by a single pixel on the plane of the sky, calculated as $A_{\text{proj}} = d^2 \cdot A_{\text{pix}}$. Here, d is the distance to the source (8.178 kpc (GRAVITY Collaboration et al. 2019)) in centimetres, and $A_{\text{pix}} = \Delta b \cdot \Delta l$ is the angular size of the pixel in steradians, where Δb and Δl are the pixel dimensions in Galactic latitude and longitude, respectively, expressed in radians. Finally, $N(\text{H}_2)$ is the column density determined using Equation 5.

3.4 Results

3.4.1 Excitation Temperature

The calculations using Equations 2 and 3 have produced a ^{13}CO LTE excitation temperature for each pixel in Fig. 1 for which a solution is possible. Fig. 3 shows the distribution of these T_{ex} values as a histogram, while Fig. 4 shows the spatial distribution extending from 5.5 K to 30 K.

The upper limit for temperatures determined using this method is approximately 200 K, as Equation 3 becomes increasingly insensitive and subject to noise fluctuations in τ_r at high temperatures. The optical-depth ratio τ_{32}/τ_{21} is less sensitive to changes in excitation temperature above ~ 50 K (see Fig. 2). The grey pixels in Fig. 4 represent positions where no valid solution could be obtained due to missing or unreliable optical depth values in one or both transitions. In bright, compact regions such as Sgr B, the τ_{13} calculation can become less accurate as high optical depths may saturate the line ratios, while calibration uncertainties and differential beam filling between the main line and isotopologue become increasingly significant at higher intensities.

The mean excitation temperature across all pixels is 12 ± 1 K. Here, the uncertainty represents the mean of the per-pixel uncertainties, derived via quadrature error propagation from τ_r . The median is 11_{-2}^{+2} K, where the uncertainties give the range covering the first and third quartiles. The highest temperatures in the CMZ are seen around the Sgr B1/B2 (G0.070–0.059) complex, where values reach $T_{\text{ex}} > 30$ K, the highest temperature is also found here at $T_{\text{ex}} > 120$ K. However, we find mostly cool temperatures across much of the CMZ, with isolated hot regions, e.g. at $\ell = 0.2^\circ$, $b = -0.1^\circ$, and $359.8^\circ \leq \ell \leq 359.6^\circ$, $b = 0^\circ$, while temperatures in Sgr A appear far cooler, with little distinction between the individual Sgr A clouds.

3.4.2 Column Density

Using the derived excitation temperatures seen in Fig. 4, we estimate the mean ^{13}CO column density to be $N(^{13}\text{CO}) = (3.0 \pm 0.5) \times 10^{16} \text{ cm}^{-2}$, where the uncertainty reflects the average per-pixel error propagated from uncertainties in T_{ex} . The median is $N(^{13}\text{CO}) = (3_{-1}^{+1}) \times 10^{16} \text{ cm}^{-2}$, the range covering the first and third quartiles.

Assuming a ^{13}CO -to- H_2 abundance ratio of $^{13}\text{CO}/\text{H}_2 = 1.29 \times 10^{-6}$, we estimate the H_2 column-density using Equation 5. Fig. 5 shows the resulting spatial distribution of the H_2 column density. The mean observed column density is $N(\text{H}_2) = (3 \pm 0.2) \times 10^{22} \text{ cm}^{-2}$, while the median is $(2_{-0.7}^{+0.9}) \times 10^{22} \text{ cm}^{-2}$, again quoting the first and third quartiles. The peak value is $2 \times 10^{25} \text{ cm}^{-2}$, located within Sgr B2.

Overall, the observed column-densities are consistent with previous

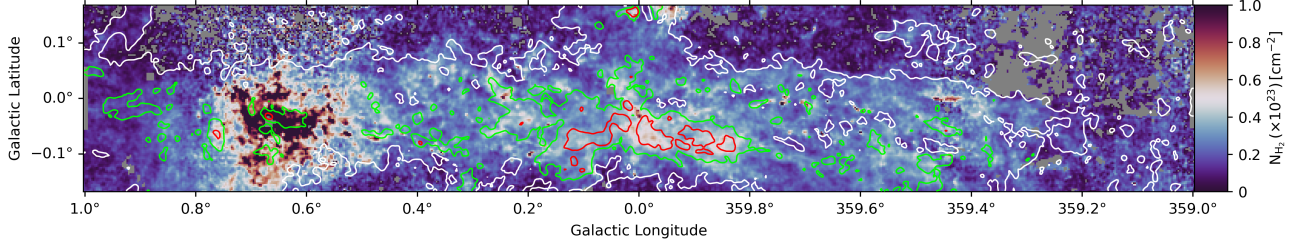


Figure 5. The H₂ column density across the CMZ. The peak column density of $2 \times 10^{25} \text{ cm}^{-2}$ is observed towards the Sgr B1/B2 complex (G0.070-0.059). The contour shows the ¹²CO $J = 3 \rightarrow 2$ peak intensity at $T_{\text{mb}} = 30 \text{ K}$ (white), 60 K (dark-grey), and 90 K (red).

CO-based (Nagai et al. 2007) and dust-continuum studies (Marsh et al. 2017; Battersby et al. 2025; Tang et al. 2021), which report similar H₂ values for the CMZ. A forthcoming paper will explore the relationship between dust and gas in the CMZ.

3.4.3 Uncertainty Estimation

To quantify the uncertainties in the derived T_{ex} and H₂ column density, we employed a Monte Carlo propagation approach. The pixel-by-pixel uncertainties in the CO line ratios were first estimated using the measured rms maps of the individual CO datasets and standard error propagation. These ratio uncertainties were then propagated to the optical depth ratio, which serves as the primary input for the excitation temperature calculation.

For each valid pixel, 1000 Monte Carlo realisations of the T_{ex} map were generated by perturbing the line ratios with Gaussian noise according to their propagated uncertainties. The excitation temperature for each realisation was computed using the same method described in section 3.2. The final T_{ex} uncertainty map was obtained as the standard deviation across all realizations, yielding a typical 1σ uncertainty of $\sim 0.58 \text{ K}$.

The T_{ex} realisations were subsequently propagated to the ¹³CO column density using Equation 4. Each realisation of $N(^{13}\text{CO})$ was converted to an H₂ column density using the same assumed abundance ratio as above. The H₂ uncertainty map was computed as the standard deviation over all Monte Carlo realisations. The median uncertainty across the map is $5.7 \times 10^{21} \text{ cm}^{-2}$, corresponding to a typical fractional uncertainty of $\sim 30\%$ relative to the median H₂ column density of $2 \times 10^{22} \text{ cm}^{-2}$.

3.4.4 Total Molecular Gas Mass

Our estimated ¹³CO-traced molecular gas mass for the observed CMZ region is $M_{\text{gas}} = (7^{+7}_{-3.5}) \times 10^6 \text{ M}_\odot$, based on the integrated H₂ column density over the inner $|\ell| < 1^\circ$ and $|b| < 0.1^\circ$. While this is lower than some previous estimates for the full CMZ, the reduced mass is expected due to our spatial coverage.

For instance, Dahmen et al. (1998) estimated a total CMZ mass of $3 \times 10^7 \text{ M}_\odot$ from C¹⁸O ($J = 1 \rightarrow 0$) observations covering a broader region ($-0.9 < |b| < 0.75$). Our estimate is therefore about a factor of 4 smaller, consistent with the smaller observed area. In contrast, Nagai et al. (2007) derived a mass of $2 \times 10^7 \text{ M}_\odot$ from a more confined region ($|b| < 0.2$), still larger than our footprint but more comparable in latitude range.

Similarly, Battersby et al. (2025) reported a dense gas mass of

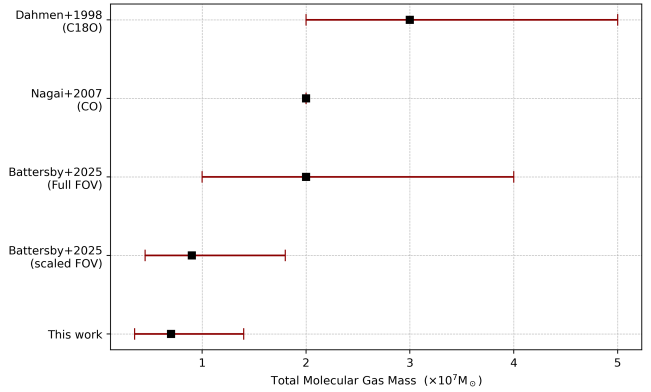


Figure 6. Total molecular gas mass estimates for the CMZ from this work and previous studies. The Battersby et al. (2025) mass estimate, originally derived from dust continuum over a larger region, has been scaled to the same effective field of view as our LTE analysis to facilitate a consistent comparison. Uncertainties for Nagai et al. (2007) are not reported in the original study and are therefore omitted here.

$M_{\text{gas}} = (2^{+2}_{-1}) \times 10^7 \text{ M}_\odot$ using *Herschel* dust-continuum observations above $N(\text{H}_2) > 10^{23} \text{ cm}^{-2}$. To enable a direct comparison despite the different spatial coverage, we scaled the Battersby et al. (2025) column-density estimate to match our observed area, thus the remaining differences in our values are primarily due to methodology and tracer sensitivity rather than field-of-view effects. When scaled, their NH₂ column-density result produces an estimated H₂ mass of $(9^{+9}_{-4.5}) \times 10^6 \text{ M}_\odot$. While our estimate is lower in absolute terms, it remains consistent with previous measurements when accounting for differences in spatial coverage, resolution, and methodology. Therefore our result supports a robust, convergent picture of CMZ molecular gas mass falling in the range $(1 - 3) \times 10^7 \text{ M}_\odot$ across studies. A comparison of these mass estimates with their reported uncertainties can be seen in Fig. 6.

In addition to the total mass across the full field, we also determine the molecular gas mass within the three major CMZ complexes individually. Using the H₂ column density within each region, we obtain $M_{\text{gas}} = 2.3 \times 10^6 \text{ M}_\odot$ for Sgr A, $3.2 \times 10^6 \text{ M}_\odot$ for Sgr B, and $1.7 \times 10^6 \text{ M}_\odot$ for Sgr C. These values reflect the well-known structural differences between the complexes: Sgr B dominates the mass budget, consistent with its extensive high-column-density gas and widespread star-forming material, whereas Sgr A and Sgr C each contribute smaller but still significant reservoirs. The relative proportions we recover shows that Sgr B contains roughly half of the total mass of the CMZ, with Sgr A and Sgr C contributing the remainder.

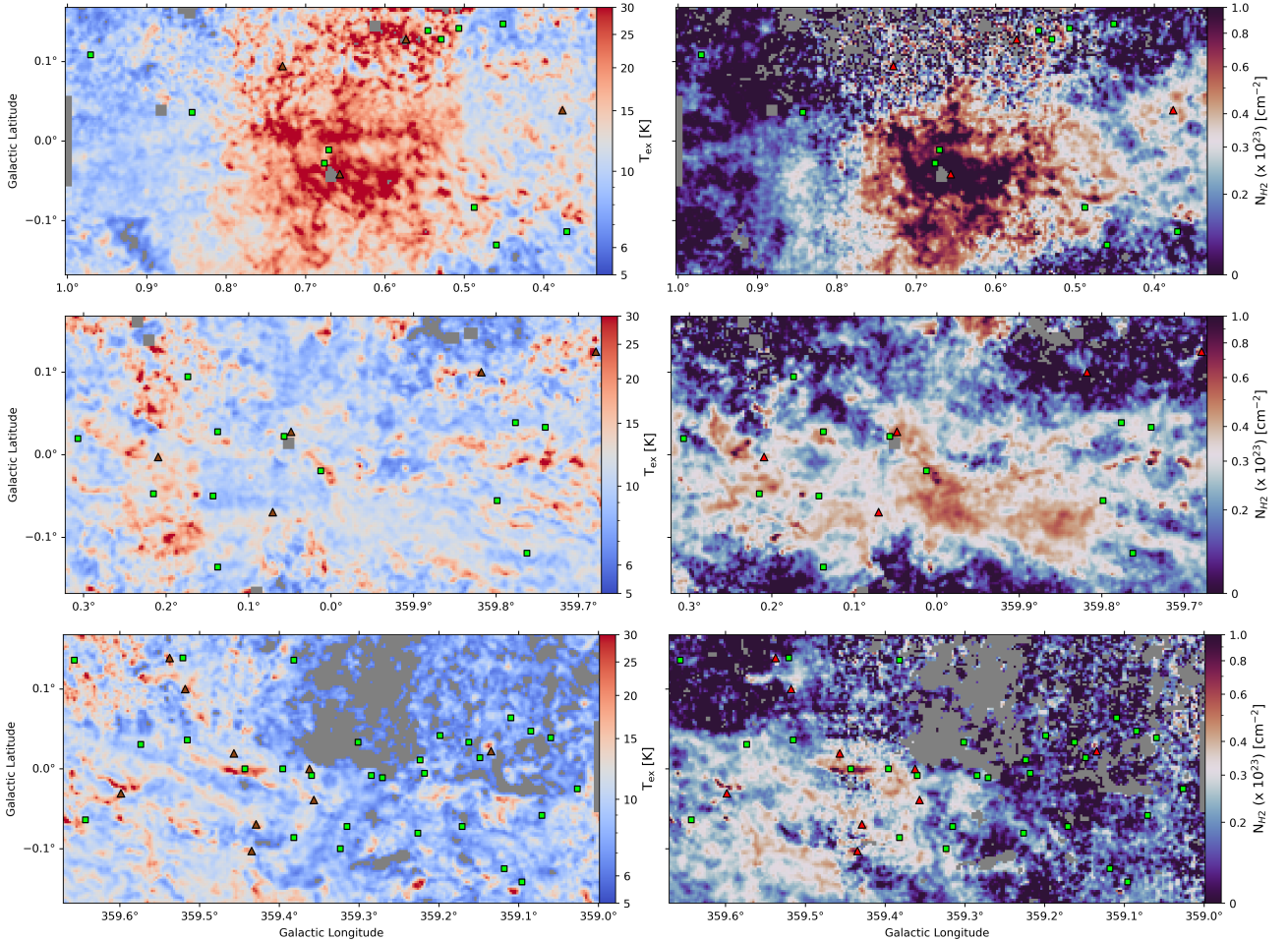


Figure 7. Comparison of the excitation temperature (left), and the H_2 column density (right) within Sgr A (middle), Sgr B (top) and Sgr C (bottom). Triangle markers show 70- μm Hi-GAL sources associated with a hotspot, while those without are shown in square markers. The temperature and column density are plotted on a logarithmic scale. This emphasizes the structural differences between them, such as those seen within the 20- km s^{-1} and 50- km s^{-1} clouds. Grey pixels represent regions where $\tau_r > 2.25$, thus no valid solution to Equation 3 is found.

3.5 Discussion

3.5.1 Excitation Temperature

We derived T_{ex} under the assumption of LTE, where the level populations of each transition are assumed to follow a Boltzmann distribution at a single temperature. Under LTE, the excitation temperature T_{ex} is expected to approach the gas kinetic temperature T_{kin} if the gas density is sufficiently high for thermalisation; here, we assume this to be the case, such that $T_{\text{ex}} = T_{\text{kin}} = T_{\text{gas}}$.

However, if the gas density is below the critical density required for collisions to dominate the excitation and the ^{13}CO ($J = 3 \rightarrow 2$) transition is sub-thermally excited, then T_{ex} may underestimate the true T_{kin} . Nevertheless, the excitation temperature reflects the relative populations in energy levels $J = 1$ to 3 . Therefore, even in sub-thermal conditions, T_{ex} should still be a reliable tracer of relative variations in T_{kin} .

The results in Fig. 4 show significant temperature variations across the CMZ. The most apparent of these is in and around the Sgr B1/B2 complex where the highest excitation temperatures are observed; here $T_{\text{ex}} > 50$ K. These high temperatures are likely to be driven by the

ongoing intense active star formation and feedback processes in this region (Schmiedeke et al. 2016; Ginsburg & Kruijssen 2018).

Temperatures are relatively lower in the Dust Ridge—a dense filamentary structure of molecular clouds extending from The Brick (G0.253+0.016) (Henshaw et al. 2019; Immer et al. 2012) towards the Sgr B1/B2 complex (G0.070-0.059), with $T_{\text{ex}} > 20$ K and several hot spots approaching ~ 50 K. This contrasts with the dust temperature of $T_{\text{dust}} < 15$ K observed in Molinari et al. (2011), as well as in Battersby et al. (2025), which reports a similar dust temperature. It has been suggested that T_{gas} and T_{dust} are thermally uncoupled (Henshaw et al. 2023), as might be expected at lower densities, and this could be responsible for the disparity between the two.

Across the wider CMZ region, the excitation temperature generally remains below 20 K. In regions such as Sgr A, the 20- km s^{-1} (G0.07–0.04) and 50- km s^{-1} (G0.06–0.07) clouds, the temperatures are similar, with minimal variation between each distinct cloud, and are similar to those shown in the dust temperature maps of Molinari et al. (2011) and Battersby et al. (2025).

Potential heating sources: To assess whether the hotspots seen in Fig. 4 and Fig. 7 are associated with identifiable heating sources, we compared the excitation temperature map with the spatial distribution

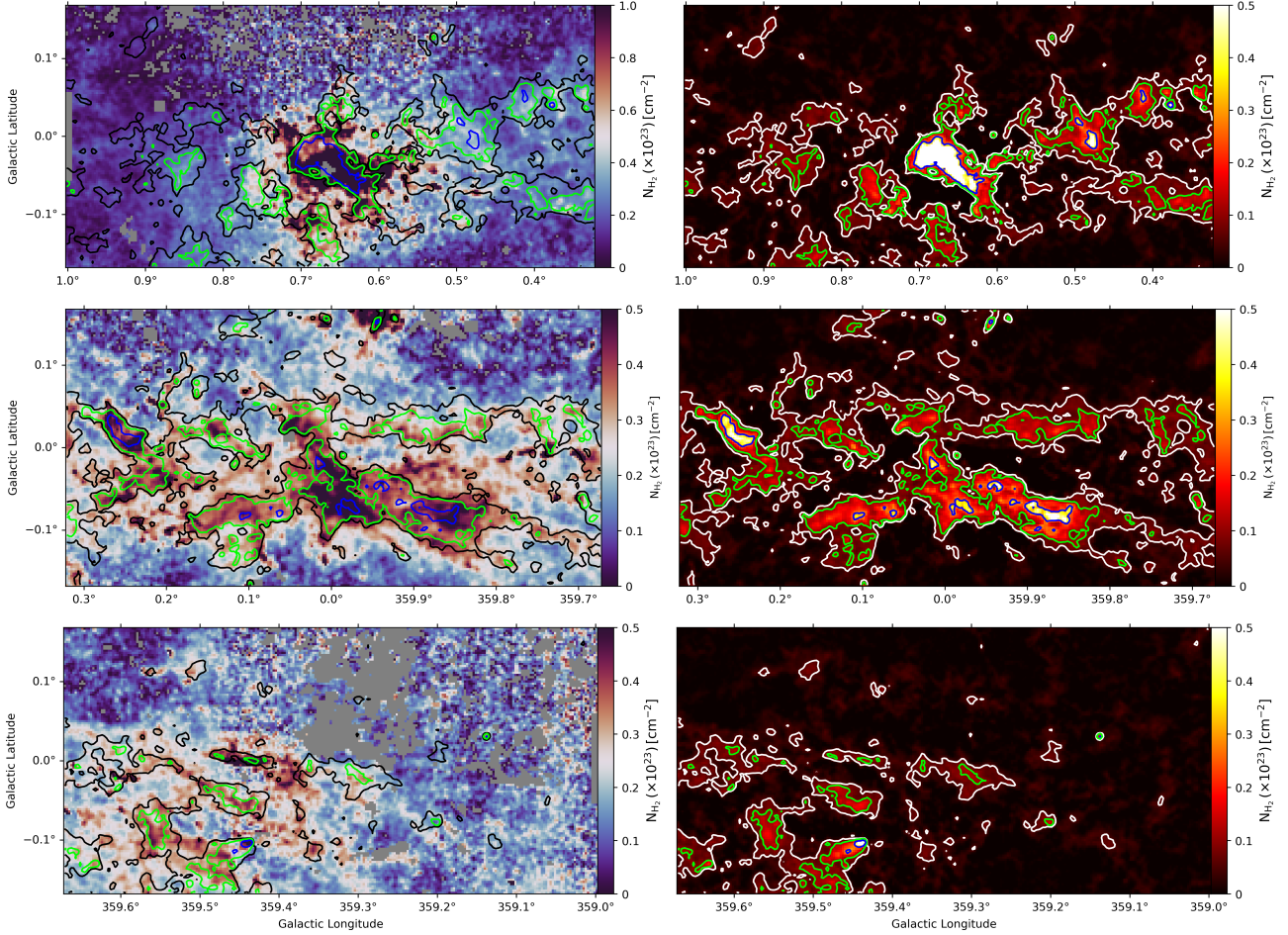


Figure 8. Comparison of the H_2 column density from this work (left) and the H_2 column density derived using the $850\text{-}\mu\text{m}$ thermal dust continuum flux density maps from SCUBA2 (Parsons et al. 2018) (right), within the regions around Sgr A (middle), Sgr B (top) and Sgr C (bottom), as in Fig. 1. Both data sets are contoured at dust-derived H_2 column densities of 0.05 (black/white), 0.1 (lime), $0.3 \times 10^{23} \text{ cm}^{-2}$ (blue).

of $70\text{-}\mu\text{m}$ sources from the Hi-GAL compact source catalogue (Elia et al. 2021). For this analysis, we assume all $70\text{-}\mu\text{m}$ sources lie at the same distance as the CMZ, consistent with the value adopted for total gas mass estimation in Section 3.3.

We identified temperature peaks as local maxima in the excitation temperature map that also lie above the 80th percentile of the temperature distribution. A $70\text{-}\mu\text{m}$ source was considered associated with a temperature peak if it lay within one beam width (30 arcsec), corresponding to the angular resolution of the excitation temperature map.

Out of approximately 70 compact $70\text{-}\mu\text{m}$ sources in the region, only 17 ($\sim 25\%$) were found within 30 arcseconds of a temperature peak after applying quality and masking criteria. These are highlighted as black/red circles in Fig. 7. The lack of association for the majority of sources suggests that $70\text{-}\mu\text{m}$ sources are not the dominant drivers of the observed excitation temperature peaks, suggesting that other heating mechanisms, such as turbulent dissipation, shocks, or cosmic rays are likely to be contributing to the heating of gas.

Localised Gas Temperature Conditions in the CMZ: A more detailed look at the LTE-temperature structure can be seen in Fig. 7. Here we present detailed T_{ex} (left column) maps across three sectors of the CMZ, each containing one of the Sagittarius complexes.

The top panel (covering $0.32^\circ < \ell < 1^\circ$) includes the Sgr B1/B2 complex and shows a highly complex temperature structure with pockets of gas that gradually become cooler outward from the region's centre. The mean temperature in the area of the figure is $T_{\text{ex}} = 14 \text{ K}$, although the temperature in Sgr B itself reaches well beyond $T_{\text{ex}} = 120 \text{ K}$ (see Fig. 7). Much of the high-temperature structure is concentrated within $0.55^\circ < \ell < 0.75^\circ$, with a narrow channel of low temperatures running horizontally through the structure at $b \approx 0.0^\circ$ which represents the separation of Sgr B2-North and Sgr B2-Main (Schmiedeke et al. 2016).

The middle panel of Fig. 7 covers the region $-0.33^\circ < \ell < 0.32^\circ$ and includes Sgr A and the 20- and 50-km s^{-1} clouds (Kauffmann et al. 2017). The temperature distribution is relatively uniform overall, but it contains a complex network of filamentary structures interspersed with compact high-temperature features. Some of these knots may correspond to embedded protostars or shock-heated regions driven by stellar feedback. While several hotspots coincide with $70\text{-}\mu\text{m}$ sources, many do not, suggesting that a variety of heating mechanisms may contribute to the observed temperature structures.

Two prominent shell-like features are visible at $\ell = 0.2^\circ$, $b = -0.1^\circ$ and $\ell = 0.2^\circ$, $b = +0.1^\circ$ in the middle panel of Fig. 7. Both exhibit partial cavities with elevated excitation temperatures along their rims and also warmer gas near their centres. Such temperature structures are

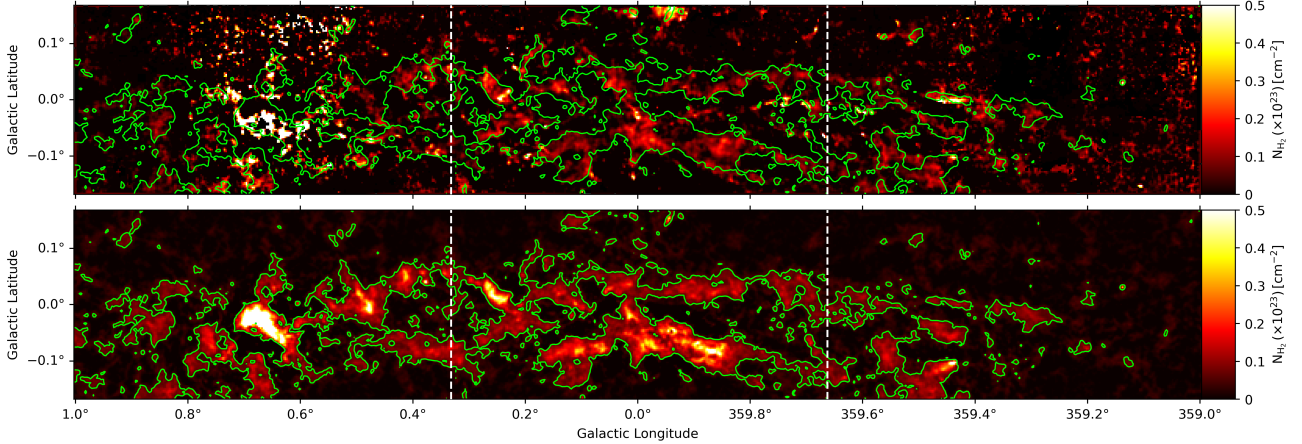


Figure 9. **Top:** The H_2 column density map shown in Fig. 5 spatially filtered to remove structures larger than ≈ 8 arcmin to match the SCUBA-2 spatial response, enabling a direct comparison between the two datasets. **Bottom:** The H_2 column density derived from the SCUBA-2 dust emission map. Both maps are overlaid with contours at $20 \text{ mJy arcsec}^{-2}$.

consistent with feedback-driven bubbles observed in other molecular environments, typically formed by OB cluster winds or protostellar outflows (Arce et al. 2011; Beaumont & Williams 2010; Barnes et al. 2017b), and supported by radiative-hydrodynamic simulations (Dale et al. 2012; Kim et al. 2023).

The lower of these two features aligns closely with the well-known 'Sickle' $\text{H}\,\text{II}$ region (G0.18–0.04), which hosts the Quintuplet Cluster and is a canonical example of stellar feedback shaping the surrounding gas (Yusef-Zadeh & Morris 1987; Lang et al. 1997; Wang et al. 2002). The morphology we observe here, a hot rim and centrally peaked T_{ex} , is consistent with this interpretation.

The upper, bow-shaped shell is located near the end of the Arches filaments and coincides with the termination point of a prominent non-thermal filament visible in MeerKAT radio continuum (Heywood et al. 2022). While its temperature morphology resembles a feedback-driven cavity, with a curved, hot rim enclosing a lower-temperature core, there is no direct positional match with the Arches Cluster itself, nor with a known $\text{H}\,\text{II}$ region. Its alignment with the filament structure suggests a possible link to large-scale dynamic processes in the CMZ, but its origin remains uncertain without clearer evidence of internal heating sources.

In the immediate vicinity of Sgr A^* ($\ell \approx 0^\circ 0, b \approx 0^\circ 0$), we see a localised elevation in excitation temperature, coinciding with a peak in H_2 column density (Fig. 7, middle panel). However, this hotspot is not associated with any nearby $70\text{-}\mu\text{m}$ source within one beam width, suggesting that it may not be heated by an embedded protostar. Instead, the elevated temperature could reflect shock heating, external irradiation from nearby clusters, or other non-localised mechanisms.

The bottom-left panel of Fig. 7, covering $359^\circ < \ell < 359.67^\circ$, shows the Sgr C region. The mean temperature here is low at $\sim 9 \text{ K}$ and features a temperature distribution similar to Sgr A . Regions of cooler temperatures prominently surround warmer, denser cores, suggesting common physical conditions across these sectors. There are prominent networks of filamentary structures, with localised peaks in excitation temperature most of which are associated with a nearby $70\text{-}\mu\text{m}$ source.

3.5.2 Column Density

The right-hand panels of Fig. 7 display the distribution of H_2 column density across the same three CMZ sectors discussed above.

In the top panel of Fig. 7, covering the region around the Sgr B1/B2 complex, we observe a peak column density of $2 \times 10^{25} \text{ cm}^{-2}$ within Sgr B2 itself, and an average value of $\sim 3 \times 10^{22} \text{ cm}^{-2}$ across the field.

The middle panel of Fig. 7 shows the region around Sgr A and the 20- and 50-km s^{-1} clouds. Here, distinct high-column-density features are apparent, more clearly separated than in the corresponding excitation temperature map. The mean column density is $2 \times 10^{22} \text{ cm}^{-2}$, with a peak of $6 \times 10^{23} \text{ cm}^{-2}$. While temperature variations are more modest, some correspondence between warm gas and high column density is evident, suggesting that heating may be associated with dense structures. However, not all dense regions exhibit elevated temperatures, consistent with expectations that ^{13}CO -traced gas can remain relatively cool. Near Sgr A^* ($\ell \sim 0^\circ 0, b \sim 0^\circ 0$), a localised column density enhancement is observed, reflecting an accumulation of dense gas near the Galactic Centre, although there is no unique feature directly identifiable with Sgr A^* itself.

In the bottom panel of Fig. 7, covering the Sgr C region ($359^\circ 67 < \ell < 359^\circ$), we observe column-density structures similar to those near Sgr A and Sgr B . Dense cores are embedded within a network of more diffuse filamentary gas, with peak column densities around $2 \times 10^{23} \text{ cm}^{-2}$.

Gas structure Validation with SCUBA-2 Dust Maps: In order to investigate the validity of the small-scale structure in the molecular-gas results through quantitative morphological tests, we compare our $N(\text{H}_2)$ result to those derived from $850\text{-}\mu\text{m}$ thermal continuum dust emission data from the JCMT SCUBA-2 survey by Parsons et al. (2018), assuming a constant dust temperature, $T_{\text{dust}} = 20 \text{ K}$, and constant dust emissivity, $\beta = 2.0$ Parsons et al. (2018). While the dust emission used to derive the total column density also traces the atomic gas phase, in the case of constant dust temperature and emissivity, and assuming the dust and gas are well mixed, the $850\text{-}\mu\text{m}$ flux density is proportional to $N(\text{H}_2)$. To convert the $850\text{-}\mu\text{m}$ emission into an H_2 column density we use the following formula.

$$N_{\text{H}_2} = \frac{I_{\nu}}{\kappa_{\nu} B_{\nu}(T) \mu_{\text{H}_2} m_{\text{H}}} \quad (7)$$

where I_{ν} is the observed 850- μm intensity, κ_{ν} is the dust opacity, $B_{\nu}(T)$ is the Planck function at dust temperature T , μ_{H_2} and m_{H} are the mean molecular weight per hydrogen molecule, and mass of a hydrogen atom, given in section 3.3.

In Fig. 8, we compare the gas-derived $N(\text{H}_2)$ result to that derived from the 850- μm thermal continuum dust emission data. Statistical analysis and by-eye comparison suggest a good degree of correspondence between the molecular gas and dust emission in regions surrounding Sgr A and Sgr C, where both the general and some small-scale structure aligns well across the maps. Some variations in the finer details can be seen, which may be attributed to differences in excitation conditions and are unlikely to be noise-related. In the region containing Sgr B1/B2, a broad correspondence is observed, but the agreement in finer details is less pronounced, this poorer correspondence could be due to variations in dust temperature or excitation conditions that violate our assumption of constant $T_{\text{dust}} = 20$ K.

To test these subjective impressions quantitatively, we have computed the two-dimensional Kolmogorov–Smirnov (KS) test (Peacock 1983) and the Spearman correlation between the full column-density map shown in Fig. 5 and the corresponding SCUBA-2 map, subset regions of which are displayed in the right-hand column of Fig. 8.

The 2D KS test extends the traditional one-dimensional KS test by comparing the empirical cumulative distribution functions (ECDFs) of two samples in two dimensions. For each pixel (x, y) , the ECDF is defined as the fraction of the total data contributed by pixels with coordinates less than or equal to (x, y) , and the test statistic is the maximum absolute difference between the ECDFs of the two datasets over all such points. This provides a measure of how similar or different the two distributions are in a spatial sense. The p-value is then estimated using the survival function of the KS distribution.

The test returned a KS statistic of 0.31 and a p-value of 0.99. This suggests that the differences between the two distributions are not statistically significant, implying that the dust emission and H_2 column density are broadly similar in their overall distribution.

The standard Spearman test was extended to two dimensions by separately calculating the pairwise correlation coefficients between the corresponding pixel values for the x and y axes of the H_2 -column-density and SCUBA-2 maps. These were then combined using Fisher's z -transformation (Fisher 1915) to obtain a single correlation coefficient that captures spatial dependencies in both directions. This method ensures that the test accounts for structure in the full two-dimensional distribution rather than treating each axis independently.

The resulting coefficient of $\rho = 0.54$ (p-value = 1.3×10^{-44}) indicates a highly significant, moderate correlation with considerable scatter. This implies that regions of higher CO-derived column density also tend to have higher 850- μm derived H_2 column-density, although the relationship is not strictly monotonic, possibly due to variations in dust temperature and emissivity (both of which were assumed constant here), or the presence of CO-dark H_2 gas. This may also be in part due to the SCUBA2 observing method and initial data reduction, the latter involving fitting to any extended background emission (which is mostly generated by the atmosphere) and removing it iteratively. This results in spatial filtering such that any emission with spatial frequencies greater than ~ 8 arcmin is suppressed; thus the comparison between our derived H_2 column-density map and the SCUBA2 map does not account for larger-scale structures.

Table 1. Statistical tests on high-pass filtered H_2 column-density maps shown in Fig. 9 by region.

Region	KS Statistic	KS p-value	Spearman ρ	p-value
Sgr A	0.62	0.83	0.50	7×10^{-11}
Sgr B	0.57	0.90	0.12	0.42
Sgr C	0.59	0.87	-0.09	2×10^{-29}
<i>Full Map</i>	0.69	0.73	0.08	0.10

To account for the spatial filtering inherent to the SCUBA-2 reduction, we repeated both statistical tests using the gas-derived H_2 column-density map after applying a Gaussian high-pass filter to remove all structure on scales larger than ~ 8 arcmin (Fig. 9). This allowed for a more direct comparison of their small-scale structure.

The 2D KS test on the filtered maps produced a KS statistic of 0.69 ($p = 0.73$), indicating that the overall spatial *distributions* of the two filtered datasets remain broadly similar, though with a larger maximum deviation between their CDFs.

In contrast, the two-dimensional Spearman correlation drops substantially once the large-scale emission is removed, yielding $\rho = 0.08$ with a non-significant $p = 0.1$. This suggests that the moderate correlation observed in the unfiltered maps is dominated by large-scale emission gradients. After matching the spatial response of the two datasets, the remaining small-scale morphology of the full map shows no statistically significant correlation.

Given this result, we performed the same filtered analysis separately on the Sgr A, B, and C regions to determine if a particular region was driving the global signal. The results are summarised in Table 1. The KS test confirms that the spatial distributions of the dust-derived and filtered gas-derived H_2 column-density maps are not significantly different in any region ($p > 0.83$ in all cases). However, the correlation behaviour varies dramatically:

- The **Sgr A** region retains a moderate but significant correlation ($\rho = 0.50$, $p \ll 0.01$).
- The **Sgr B** region shows no significant correlation ($\rho = 0.12$, $p = 0.42$), consistent with the visual impression that its gas emission is dominated by large-scale structures not present in the SCUBA-2 data.
- The **Sgr C** region shows a significant but very weak *anti*-correlation ($\rho = -0.09$, $p \ll 0.01$).

This regional decomposition reveals that the lack of a significant global correlation in the filtered maps is primarily due to the Sgr B region, which dominates the total area. The strong correlation in Sgr A is washed out in the whole-map analysis, indicating that the relationship between dust emission and gas tracers is not uniform across the Galactic Centre.

4 STAR FORMATION EFFICIENCY IN THE CMZ

In a previous work (King et al. 2024), we examined the relationship between the distribution of compact Hi-GAL sources and that of the molecular gas traced by ^{13}CO in the CMZ. We found that 70- μm -bright sources, which are typically associated with actively star-forming regions, tend to be less spatially correlated with the dense molecular gas, suggesting that many of these sources may be located in foreground spiral arms rather than within the CMZ itself.

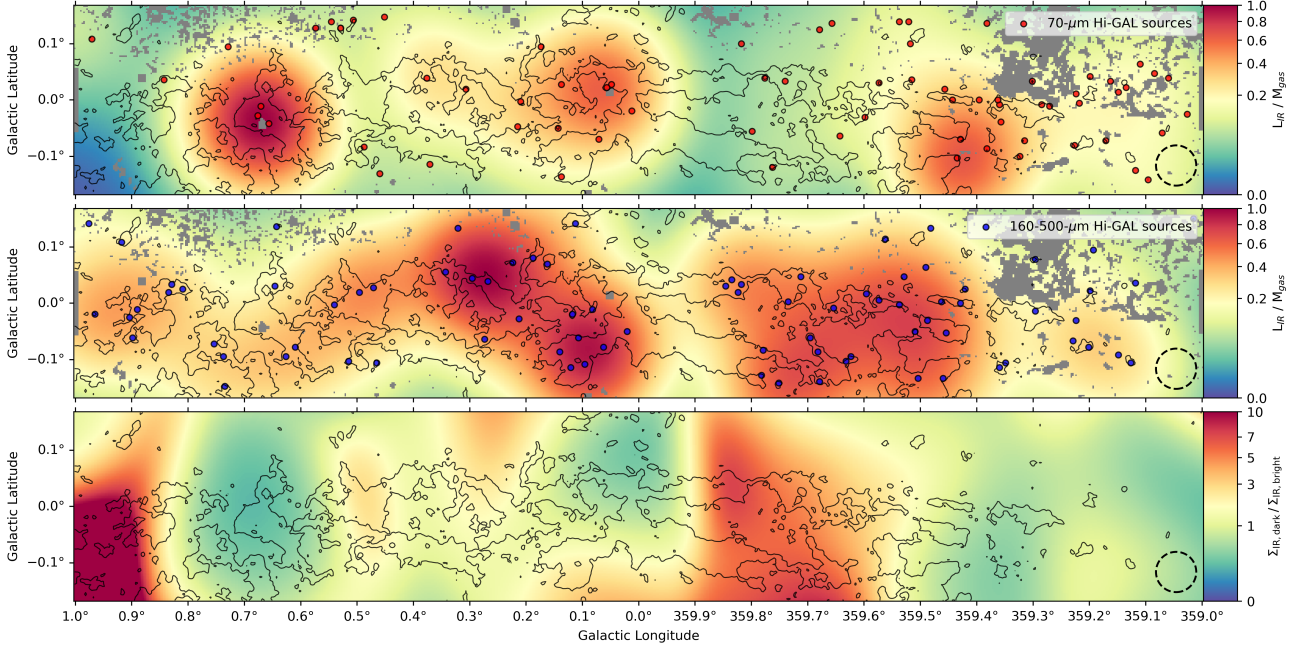


Figure 10. Top: The normalised star formation efficiency for the CMZ using 70- μm sources (red circles) from HiGAL (Molinari et al. 2016; Elia et al. 2021). **Middle:** As for the top panel but showing the star formation efficiency using sources detected at 160–500- μm but not at 70- μm (blue circles). **Bottom:** The luminosity surface-density ratio, low values indicate regions nearing the end of their star forming phase. A luminosity surface-density ratio equal to 1 represents no significant relative change in SFE over time. The contours show the SCUBA2 dust emission at 20 (black) mJy arcsec $^{-2}$. The black circles in the bottom right represent the respective smoothing scale applied to the H₂ column-density maps. Grey pixels here represent values which returned a NaN, thus no valid solution to Equation 8 is found.

In contrast, 160-500- μm sources without 70- μm detections, which may represent earlier stages of star formation, showed a stronger correlation with the ¹³CO spatial distribution, suggesting a closer association with the dense molecular gas in the CMZ. This gives us important context for evaluating the star formation efficiency (SFE) across the CMZ.

The instantaneous SFE can be defined as the fraction of mass in dense CO-traced clouds that has formed stars over a given timescale (Eden et al. 2015). However, as the stellar mass cannot be measured directly, the luminosity of Young Stellar Objects (YSOs) embedded within these clouds serves as an indirect measure of their star formation activity. Therefore, the SFE can be parameterised by the ratio of the bolometric infrared (IR) luminosity of YSOs to the mass of molecular gas (Urquhart et al. 2013), given by:

$$SFE = \frac{L_{\text{IR}}}{M_{\text{gas}}} = \frac{1}{M_{\text{gas}}} \cdot \int_0^t \frac{dL}{dt} dt \quad (8)$$

This is equivalent to the ratio of the infrared surface brightness (Σ_{IR}) to the column density of molecular hydrogen ($N(\text{H}_2)$), as long as the angular resolution or sampling scale is the same for both measurements. This ratio is independent of distance, meaning that the presence of different, often unreliable, distances for the clouds in the data does not affect our results, although overlapping line-of-sight features will be merged in the result because of this.

It is important to note that we are not deriving absolute values of SFE, in terms of a fractional mass, but are using the $L_{\text{IR}}/M_{\text{gas}}$ parameter as a proxy to trace relative variations in SFE across different regions.

Given that the bolometric luminosity of infrared sources, L_{IR} , does not scale linearly with the total stellar mass, the luminosity of young

stellar objects (YSOs) is influenced not only by their mass but also by their evolutionary stage and accretion rate. In the early phases of star formation, the luminosity is dominated by accretion processes, leading to significant variation among individual YSOs. For a fully populated initial mass function (IMF), the total luminosity of main-sequence stars follows a relation of $L \propto M^{-3.5}$ for individual stars, and $L \propto M^2$ for clusters (Eden et al. 2015). However, this relationship may be altered depending on whether the IMF is fully sampled. Here, we assume that it is, and that evolutionary timescales are short compared to the lifetime of a molecular cloud. We further assume that the infrared luminosity is primarily driven by high-mass main-sequence or near-main-sequence stars, which have already undergone most of their luminosity evolution. As a result, their brightness remains relatively stable during the IR-luminous phase (Urquhart et al. 2022).

The infrared luminosity, L_{IR} , is derived from the integrated continuum fluxes of YSOs detected by Hi-GAL across multiple wavelengths, while the gas mass, M_{gas} , is obtained from CO-traced observations of the molecular gas. These two quantities are independently measured and derived through distinct observational techniques, and thus exhibit no inherent correlation beyond their physical connection via the star formation process. The ratio $L_{\text{IR}}/M_{\text{gas}}$ can inherently reflect evolutionary effects, particularly when evaluated for individual sources or when both L and M are derived from the same continuum measurements. However, we argue that the 70- μm -bright and -dark phases (those traced by 160–500- μm sources) are expected to be relatively short-lived compared to overall cloud lifetimes and are here averaged over statistically large samples, therefore the resulting $L_{\text{IR}}/M_{\text{gas}}$ maps robustly reflect the instantaneous star-formation efficiency in each phase, and comparison between the phases provides information on evolution.

4.1 Method

We have adopted a surface-density based approach rather than segmenting the CMZ into discrete molecular clouds. This method allows us to trace large-scale spatial variations in SFE across the CMZ without imposing an artificial division into clouds, which can be strongly dependent on the choice of cloud identification algorithm and input parameter values. By correlating the infrared luminosity surface density produced by compact sources with gas mass surface density on a pixel-by-pixel basis, we are able to probe the variations in $L_{\text{IR}}/M_{\text{gas}}$ throughout the CMZ.

We conducted our analysis using all five Hi-GAL wavebands (70, 160, 250, 350 and 500 μm) from the [Elia et al. \(2021\)](#) compact-source catalogue. 70- μm emission serves as a tracer of active star formation within dense cores, while the longer-wavelength submillimetre bands (160 to 500- μm) probe dense, cold structures associated with embedded star-forming regions. Although bolometric luminosities for Hi-GAL clumps are available in the [Elia et al. \(2021\)](#) catalogue, we opted to compute luminosities using only these five Hi-GAL wavelengths, excluding shorter-wavelength fluxes (21–24- μm) that may be dominated by transiently heated dust, as well as longer wavelengths (870–1100 μm) that may trace more extended cold dust unrelated to compact dense cores.

The SFE analysis focused on the ratio of the bolometric infrared luminosity (L_{IR}) of Hi-GAL sources to the gas mass estimated using Equation 6 at each pixel in H_2 column density in Fig. 5. L_{IR} is given by:

$$L_{\text{IR}} = 4\pi d^2 \int_{\nu_{\text{min}}}^{\nu_{\text{max}}} S_{\nu} d\nu. \quad (9)$$

where S_{ν} is the flux density, ν_{min} and ν_{max} are the Hi-GAL wavelengths converted to the frequency domain and d is the distance. In practice we only require the integrated flux, since the ratio of this to the mass column density gives us $L_{\text{IR}}/M_{\text{gas}}$ without the need to define actual source distances. We employed the trapezium method to numerically approximate the integral.

To calculate a continuous bolometric luminosity surface density distribution from the discrete Hi-GAL sources, we used a Gaussian Kernel Density Estimation (KDE). The smoothing scale was determined using Silverman's rule of thumb for bandwidth estimation ([Silverman 1986](#)), given by:

$$h = \left(\frac{4\langle\sigma\rangle^5}{3n} \right)^{1/5}, \quad (10)$$

where $\langle\sigma\rangle$ is the standard deviation of the source coordinates along one spatial axis, and n is the number of data points (i.e., the number of 70- μm and 160–500- μm Hi-GAL compact sources). While Silverman's rule is traditionally applied by averaging the spread across both axes (assuming isotropy), in our case the spatial distribution of sources is highly anisotropic, with a significantly narrower spread along Galactic latitude. We therefore adopted a more representative, symmetric smoothing scale by applying twice the bandwidth estimated from the latitude axis alone ($2h_y$), thereby avoiding excessive smoothing along the more extended longitude direction, and to avoid zeros in the resulting interpolation.

This smoothing scale (equivalent to $2h_y$) was applied to the H_2 column-density map (Fig. 5) to match the effective resolution of the surface-luminosity maps (see lower two panels of Fig. A1). As this

smoothing scale is coarser than the native resolution of the H_2 map, small-scale variations in SFE are not resolved. In any case, there is a minimum scale below which the concept of SFE becomes meaningless. As such, our analysis focuses on the larger-scale structure of the star formation efficiency distribution.

To produce the SFE maps shown in Fig. 10, the Hi-GAL surface luminosity was divided by the smoothed H_2 column density to produce two distinct SFE distributions: one for actively star-forming regions ([Moore et al. 2012; Eden et al. 2015](#)), and another for those apparently at earlier stages of evolution ([Eden et al. 2012; Eden et al. 2013](#)).

4.2 Results

Fig. 10 shows the distribution of the SFE, defined as $L_{\text{IR}}/M_{\text{gas}}$, across the CMZ. The values are normalised to a common scale to emphasise relative variation rather than absolute efficiency. The top panel traces the SFE derived from 70- μm -bright sources, representing a snapshot of current star formation activity, while the bottom panel shows the instantaneous SFE based on 160–500- μm sources, indicative of potential future star formation assuming that these regions will eventually form stars.

In the top panel, the 70- μm -bright SFE is enhanced in three well-known regions. We observe elevated SFE in the Sgr B1/B2 complex (G0.070–0.059), consistent with its well-established role as one of the most active star-forming regions in the Galaxy. Sgr B2 in particular has been the subject of extensive study due to its exceptional mass, density, and ongoing high-mass star formation (e.g., [Ott et al. 2014; Ginsburg et al. 2018; Ginsburg & Kruijssen 2018; Mills et al. 2018; Schwörer et al. 2019; Santa-Maria et al. 2021](#)). Elevated SFE is also seen in the vicinity of the Arches cluster (G0.121+0.017) and in Sgr C (G-0.49–0.130), although not to the same extent as in Sgr B1/B2. These enhancements are consistent with previous studies identifying these regions as significant sites of star formation in the CMZ (e.g., [Figer et al. 2002; Kendrew et al. 2013](#)).

Slightly elevated SFE is also observed across the dust ridge clouds (G0.20+0.003), particularly to the left of the Arches cluster, with the exception of clouds e&f (G0.490+0.008), which display significantly lower SFE compared to the other dust ridge clouds (clouds b, c, d, and the Brick). This forms a notable boundary of low SFE between the dust ridge and the Sgr B1/B2 complex.

The middle panel shows a contrasting distribution. The 160–500- μm -derived SFE appears elevated across much of the CMZ, but is notably lower toward the Sgr B1/B2 complex compared to the 70- μm -bright SFE in the top panel. This reduction was initially attributed to saturation in the 160- and 250- μm PACS bands, which are known to saturate in high surface-brightness regions such as Sgr B2 ([Poglitsch et al. 2010; Griffin et al. 2010](#)). However, since both subsets of the surface luminosity used to derive the SFE (top and middle panels) include the 160- and 250- μm bands, any impact from saturation is present in both maps. Whereas, the 350- and 500- μm SPIRE bands are not significantly affected and continue to trace cold, extended emission.

Therefore, the observed drop in SFE in the middle panel is not an artifact of saturation, but probably reflects a genuine decrease in the number or luminosity of cold embedded Hi-GAL sources in Sgr B2. This suggests a lower star-formation efficiency in the future. This interpretation is further supported by the surface-luminosity ratio map in the lower panel of Fig. 10, which highlights regions where current star formation is elevated relative to cold dust reservoirs. Regions such as Sgr B2 with high surface-luminosity ratios are con-

sistent with being towards the end of their star-forming lifetimes. This is further supported by the surface-luminosity ratio map in the lower panel of Fig. 10. Since this ratio is proportional the ratio of the two SFE values, it highlights regions where current SFE is reduced relative to the available gas reservoir. Regions such as Sgr B2 with low ratios are therefore consistent with being toward the end of their star-forming lifetimes.

The SFE across the dust ridge clouds is significantly elevated in this map compared to the 70- μm -bright counterpart, with the Brick and the Three Little Pigs clouds (G0.110-0.079) now showing comparably high SFEs. SFE also remains high toward Sgr C, as in the 70- μm map, but is now more spatially extended, including the Wiggles feature (Henshaw et al. 2020) and surrounding clouds.

4.3 Discussion

The $L_{\text{IR}}/M_{\text{gas}}$ values in Fig. 10 are shaped by two main factors: the star formation rate (SFR) per unit gas mass, integrated over a relevant timescale, and the luminosity function (LF) of embedded young stellar sources. In this study, the timescale is constrained by the evolutionary phases traced by Hi-GAL: 70- μm -bright sources associated with protostars ($< 5 \times 10^5$ yr; Mottram et al. 2011) and cold dust structures or prestellar cores detected only at longer wavelengths (typically $\sim 3 \times 10^5$ yr; Kirk et al. 2005). These timescales are significantly shorter than the typical lifetimes of molecular clouds ($\sim 10^7$ – 5×10^7 yr; Jeffreson & Krijssen 2018), so $L_{\text{IR}}/M_{\text{gas}}$ effectively traces a snapshot of the current or near-future star formation activity.

The two SFE maps in Fig. 10 capture complementary stages in the star formation cycle. The 70- μm -bright sources trace ongoing, embedded star formation, while the sources detected only at longer wavelengths (160–500 μm) represent colder, denser structures that have not yet formed protostars such as pre-stellar cores, filaments, or clumps. Their associated instantaneous SFE thus represents an incipient or potential future star formation efficiency.

A significant feature of Fig. 10 is the spatial contrast between the upper two maps. The bottom panel provides insight into the relative evolutionary potential of the SFE through the ratio of the luminosities shown in Fig. A1. A value of 1 represents no potential change in SFE over time, thus regions such as Sgr B1/B2, are likely to be at the end of their star-forming phase. A higher value represents regions with an elevated potential for future star formation, such as the dust ridge clouds and Sgr C, which exhibit modest SFE distributions in the 70- μm -bright map but show significantly higher values in the 160–500 μm map. Conversely, areas with elevated current star formation — particularly Sgr B1/B2 — show a suppressed incipient SFE. This relative anti-correlation suggests a spatial variation in evolutionary stage: while some regions are currently active, others may be on the verge of entering a more intense star-forming phase.

Despite hosting a large gas reservoir and known luminous sources, the Sgr B1/B2 complex exhibits relatively low SFE in the 160–500 μm map. This may reflect the combined effects of turbulent cloud kinematics (Henshaw et al. 2016a) and elevated gas temperatures (Ginsburg et al. 2016), both of which can inhibit the collapse of dense structures. Alternatively, it may indicate that this region is transitioning out of a star-forming phase and entering a more quiescent evolutionary state.

Together, these findings suggest that while the CMZ exhibits localised sites of intense star formation (e.g., Sgr B2, Arches), it also harbours a widespread reservoir of cold, dense gas with the potential for future activity. This is quantitatively supported by the higher average incip-

ient SFE in the 160–500- μm derived map ($SFE = 0.35$) compared to the current SFE shown in the 70- μm bright map ($SFE = 0.19$), suggesting we may be observing during a low-activity period preceding more widespread star formation.

The elevated incipient SFE across the dust ridge clouds, Sgr C, and in the Sgr A region shown in the lower panel of Fig. 10 implies that a broader starburst phase may be imminent across the CMZ and we may be observing during a low-activity period.

Source distance considerations: We assume that all sources presented here are physically located within the CMZ. Although precise distance measurements are lacking, the strong concentration of sources in Galactic latitude, combined with the known spread of foreground spiral arm emission in the CHIMPS2 data (Eden et al. 2020; King et al. 2024), supports this assumption. A small fraction of contamination from foreground structures cannot be ruled out, but is unlikely to significantly affect the overall trends discussed here.

5 SUMMARY

We present an analysis of molecular gas properties and star formation activity in the CMZ, revealing several key findings:

The LTE gas temperature map across the CMZ shows a mean temperature of 12 ± 6 K and a median of 11^{+2}_{-2} K, with the highest temperatures exceeding 30 K observed around Sgr B (G0.68-0.05), and $T_{\text{ex}} > 120$ K within Sgr B. In contrast, gas temperatures near Sgr A appear significantly cooler with little variation in temperature among individual clouds, though overall the temperatures traced by ^{13}CO appear consistent with dust temperatures presented in Molinari et al. (2011). Excitation temperatures reveal a significant and extended filamentary structure surrounding Sgr A clouds, and in negative longitudes towards Sgr C.

Our column density estimates reveal a median ^{13}CO column density of $(3^{+1}_{-1}) \times 10^{16} \text{ cm}^{-2}$, corresponding to an H_2 column density of $(2^{+0.9}_{-0.7}) \times 10^{22} \text{ cm}^{-2}$. The highest column density, $2 \times 10^{25} \text{ cm}^{-2}$, is also found near Sgr B2, which coincides with its status as a prominent site of star formation. The total ^{13}CO -traced mass in the CMZ is estimated to be $M_{\text{gas}} = (7^{+7}_{-3.5}) \times 10^6 M_{\odot}$, the upper limit of our estimate is consistent with Dahmen et al. (1998), while our total estimate is consistent with Nagai et al. (2007) and Battersby et al. (2025). These agreements suggest that the total mass of the CMZ is well-established within these limits.

Mapping the instantaneous star formation efficiency (SFE) using Hi-GAL sources reveals clear spatial variations that distinguish between current and potential future star-forming regions in the CMZ. In the 70- μm -bright map, which traces embedded, actively star-forming sources, the SFE is enhanced in several known regions, including the Sgr B1/B2 complex, the Arches cluster, and Sgr C. Modest enhancement is also seen across the dust ridge clouds. However, the overall distribution of SFE in dust ridge clouds remains relatively low compared to other regions such as the nearby Arches cluster.

In contrast, the SFE traced by 160–500- μm sources, which probe colder dust and prestellar structures shows a much broader and more uniform enhancement across the CMZ. This includes high values in the Brick, the Three Little Pigs clouds, the Arches region, and throughout both high and low latitudes, particularly at negative longitudes towards the Sgr C region. These features suggest the presence of widespread, dense gas that is potentially on the verge of forming stars. Interestingly, Sgr B1/B2 shows relatively low SFE in 160–500-

μm tracers, despite its substantial gas reservoir. This may reflect physical conditions, such as turbulent kinematics and high gas temperatures—that inhibit gravitational collapse, or it may indicate that the region is evolving into a more quiescent phase.

Together, these maps support a dynamic evolutionary scenario for star formation in the CMZ. The widespread elevation of 160–500- μm SFE across quiescent clouds and inflow regions suggests that the CMZ is primed for a future increase in star formation activity, consistent with models of orbital inflow and cloud evolution. The contrasting morphologies between the two maps shows a clear progression from dense, cold gas to luminous protostellar activity, linking the observed SFE distribution to the larger dynamical cycle of gas inflow, accumulation, and star formation in the Galactic Centre.

ACKNOWLEDGEMENTS

The James Clerk Maxwell Telescope is operated by the East Asian Observatory on behalf of The National Astronomical Observatory of Japan; Academia Sinica Institute of Astronomy and Astrophysics; the Korea Astronomy and Space Science Institute; the Operation, Maintenance and Upgrading Fund for Astronomical Telescopes and Facility Instruments, budgeted from the Ministry of Finance (MOF) of China and administrated by the Chinese Academy of Sciences (CAS). Additional funding support is provided by the Science and Technology Facilities Council of the United Kingdom and participating universities in the United Kingdom and Canada. The Starlink software (Currie et al. 2014) is currently supported by the East Asian Observatory. This research has made use of NASA’s Astrophysics Data System.

This publication is based in part on data acquired with the Atacama Pathfinder Experiment (APEX) under programmes 092.F-9315 and 193.C-0584. APEX is a collaboration among the Max-Planck-Institut fur Radioastronomie, the European Southern Observatory, and the Onsala Space Observatory.

DATA AVAILABILITY

The reduced CHIMPS2 ^{13}CO CMZ data are available to download from the [CANFAR archive](#). The data are available as mosaics, roughly $2^\circ \times 1^\circ$ in size, as well as individual observations. The data are presented in FITS format.

The processed SEDIGISM data products are available from the [SEDIGISM database](#), which was constructed by James Urquhart and hosted by the Max Planck Institute for Radio Astronomy.

REFERENCES

Arce H. G., Borkin M. A., Goodman A. A., Pineda J. E., Halle M. W., 2011, *The Astrophysical Journal*, 742, 105

Barnes A. T., Longmore S. N., Battersby C., Bally J., Kruijssen J. M. D., 2017b, *Monthly Notices of the Royal Astronomical Society*, 469, 2263

Barnes A. T., Longmore S. N., Battersby C., Bally J., Kruijssen J. M. D., Henshaw J. D., Walker D. L., 2017a, *Monthly Notices of the Royal Astronomical Society*, 469, 2263

Battersby C., et al., 2025, *ApJ*, 984, 156

Beaumont C. N., Williams J. P., 2010, *The Astrophysical Journal*, 709, 791

Buckle J. V., et al., 2009, *MNRAS*, 399, 1026

Currie M. J., Berry D. S., Jenness T., Gibb A. G., Bell G. S., Draper P. W., 2014, in Manset N., Forshay P., eds, Astronomical Society of the Pacific Conference Series Vol. 485, Astronomical Data Analysis Software and Systems XXIII. p. 391

Dahmen G., Huttemeister S., Wilson T. L., Mauersberger R., 1998, *A&A*, 331, 959

Dale J. E., Ercolano B., Bonnell I. A., 2012, *Monthly Notices of the Royal Astronomical Society*, 424, 377

Dale J. E., Diederik Kruijssen J., Longmore S. N., 2019, *Monthly Notices of the Royal Astronomical Society*, 486, 3307

Eden D. J., Moore T. J., Plume R., Morgan L. K., 2012, *MNRAS*, 422, 3178

Eden D. J., Moore T. J. T., Morgan L. K., Urquhart J. S., Thompson M. A., 2013, *MNRAS*, 431, 1587

Eden D. J., Moore T. J. T., Urquhart J. S., Elia D., Plume R., Rigby A. J., Thompson M. A., 2015, *MNRAS*, 452, 289

Eden D. J., et al., 2020, *MNRAS*, 498, 5936

Elia D., et al., 2017, *Monthly Notices of the Royal Astronomical Society*, 471, 100

Elia D. Q., Merello M., Molinari S., Schisano E., Zavagno A., et al. 2021, *Monthly Notices of the Royal Astronomical Society*, 504

Ferrière K., Gillard W., Jean P., 2007, *A&A*, 467, 611

Figer D. F., et al., 2002, *The Astrophysical Journal*, 581, 258

Fisher R. A., 1915, *Biometrika*, 10, 507

GRAVITY Collaboration et al., 2019, *A&A*, 625, L10

Ginsburg A., Kruijssen J. M. D., 2018, *The Astrophysical Journal*, 864, L17

Ginsburg A., et al., 2016, *Astronomy & Astrophysics*, 586, A50

Ginsburg A., et al., 2018, *ApJ*, 853, 171

Griffin M. J., et al., 2010, *Astronomy & Astrophysics*, 518, L3

Güsten R., Nyman L. Å., Schilke P., Menten K., Cesarsky C., Booth R., 2006, *A&A*, 454, L13

Henshaw J. D., et al., 2016a, *MNRAS*, 457, 2675

Henshaw J. D., Longmore S. N., Ginsburg A., Barnes A. T., Jackson J. M., 2016b, *Monthly Notices of the Royal Astronomical Society*, 463, L122

Henshaw J. D., et al., 2019, *MNRAS*, 485, 2457

Henshaw J. D., et al., 2020, *Nature Astronomy*, 4, 1064–1071

Henshaw J., Barnes A., Battersby C., Ginsburg A., Sormani M., Walker D., 2023, in Protostars and Planets VII - Conference. Kyoto, Japan

Heywood I., et al., 2022, *The Astrophysical Journal*, 925, 165

Immer K., Schuller F., Omont A., Menten K. M., Gouliermis D. A., 2012, *Astronomy & Astrophysics*, 537, A121

Jackson J. M., et al., 2006, *The Astrophysical Journal Supplement Series*, 163, 145

Jeffreys S. M. R., Kruijssen J. M. D., 2018, *Monthly Notices of the Royal Astronomical Society*, 476, 3688

Kauffmann J., Bertoldi F., Bourke T. L., Evans II N. J., Lee C. W., 2008, *A&A*, 487, 993

Kauffmann J., Pillai T., Zhang Q., Menten K. M., Goldsmith P. F., Lu X., Guzmán A. E., 2017, *A&A*, 603, A89

Kendrew S., Ginsburg A., Johnston K., Beuther H., Bally J., Cyganowski C. J., Battersby C., 2013, *The Astrophysical Journal*, 775, L50

Kim C.-G., Ostriker E. C., Kim J., 2023, *The Astrophysical Journal*, 942, 25

King S. M., et al., 2024, *MNRAS*, 533, 131

Kirk J. M., Ward-Thompson D., André P., 2005, *Monthly Notices of the Royal Astronomical Society*, 360, 1506

Krieger N., et al., 2017, *ApJ*, 850, 77

Kruijssen J. M. D., Longmore S. N., Elmegreen B. G., Murray N., Bally J., Testi L., Kennicutt R. C. J., 2014, *Monthly Notices of the Royal Astronomical Society*, 440, 3370

Lada C. J., Forbrich J., Lombardi M., Alves J. F., 2012, *ApJ*, 745, 190

Lang C. C., Goss W. M., Wood D. O. S., Hyman S. D., 1997, *The Astrophysical Journal*, 474, 275

Longmore S. N., et al., 2013, *MNRAS*, 429, 987

Marsh K. A., et al., 2017, *Monthly Notices of the Royal Astronomical Society*, 471, 2730

Mills E. A. C., 2017, arXiv preprint arXiv:1705.05332

Mills E. A. C., Butterfield N., Ludovici D. A., Lang C. C., Ott J., Morris M. R., Walker D. L., Mills M. S., 2018, *The Astrophysical Journal*, 868, 7

Mizuno I., et al., 2020, in Zmuidzinas J., Gao J.-R., eds, Society of Photo-Optical Instrumentation Engineers (SPIE) Conference Series Vol. 11453, Millimeter, Submillimeter, and Far-Infrared Detectors and Instrumentation for Astronomy X. p. 11453T (arXiv:2012.07349), doi:10.1117/12.2561742

Molinari S., et al., 2011, *ApJ*, 735, L33

Molinari S., et al., 2016, [A&A](#), **591**, A149

Moore T. J. T., Urquhart J. S., Morgan L. K., Thompson M. A., 2012, [MNRAS](#), **426**, 701

Morris M., Serabyn E., 1996, [ARA&A](#), **34**, 645

Mottram J. C., et al., 2011, [The Astrophysical Journal Letters](#), **730**, L33

Nagai M., Tanaka K., Kamegai K., Oka T., 2007, [/pasj](#), **59**, 25

Nakanishi H., Sofue Y., 2006, [PASJ](#), **58**, 847

Oka T., Hasegawa T., Sato F., Tsuboi M., Miyazaki A., 1998, [ApJS](#), **118**, 455

Ott J., Weiß A., Staveley-Smith L., Henkel C., Meier D. S., 2014, [The Astrophysical Journal](#), **785**, 55

Parsons H., et al., 2018, [ApJS](#), **234**, 22

Peacock J. A., 1983, [MNRAS](#), **202**, 615

Poglitsch A., et al., 2010, [Astronomy & Astrophysics](#), **518**, L2

Rathborne J. M., Johnson A. M., Jackson J. M., Shah R. Y., Simon R., 2009, [ApJS](#), **182**, 131

Rathborne J. M., et al., 2014, [ApJ](#), **786**, 140

Santa-Maria M. G., Goicoechea J. R., Etxaluze M., Cernicharo J., Cuadrado S., 2021, [Astronomy & Astrophysics](#), **649**, A32

Schmiedeke A., Schilke P., Lis D. C., Qiu K., Comito C., Rolffs R., Thorwirth S., 2016, [Astronomy & Astrophysics](#), **588**, A143

Schuller F., et al., 2017, [A&A](#), **601**, A124

Schwörer A., et al., 2019, [Astronomy & Astrophysics](#), **628**, A6

Silverman B. W., 1986, Density Estimation for Statistics and Data Analysis. Monographs on Statistics and Applied Probability Vol. 26, Chapman & Hall/CRC, London

Tang Y., Wang Q. D., Wilson G. W., 2021, [Monthly Notices of the Royal Astronomical Society](#), **505**, 2377

Urquhart J. S., et al., 2013, [MNRAS](#), **431**, 1752

Urquhart J. S., et al., 2022, [Monthly Notices of the Royal Astronomical Society](#), **510**, 3389

Wang Q. D., Gotthelf E. V., Lang C. C., 2002, [Nature](#), **415**, 148

Yusef-Zadeh F., Morris M., 1987, [The Astrophysical Journal](#), **320**, 545–561

APPENDIX A: SMOOTHED HI-GAL SURFACE LUMINOSITY AND H₂ COLUMN-DENSITY PLOTS

The top two panels of Fig. A1 show the smoothed surface luminosity distribution of Hi-GAL sources, used to derive the luminosity-to-mass ($L_{\text{IR}}/M_{\text{gas}}$) in the main SFE analysis. The map shows the spatially smoothed luminosity surface density of compact sources detected at 70 μm (top panel) and 160–500 μm (second panel).

The lower two panels of Fig. A1 show the H₂ column-density map (see Fig. 5) smoothed to the 8.5 arcmin resolution of the surface luminosity map. These maps serve as the basis for calculating the SFE maps shown in Fig. 10.

This paper has been typeset from a $\text{\TeX}/\text{\LaTeX}$ file prepared by the author.

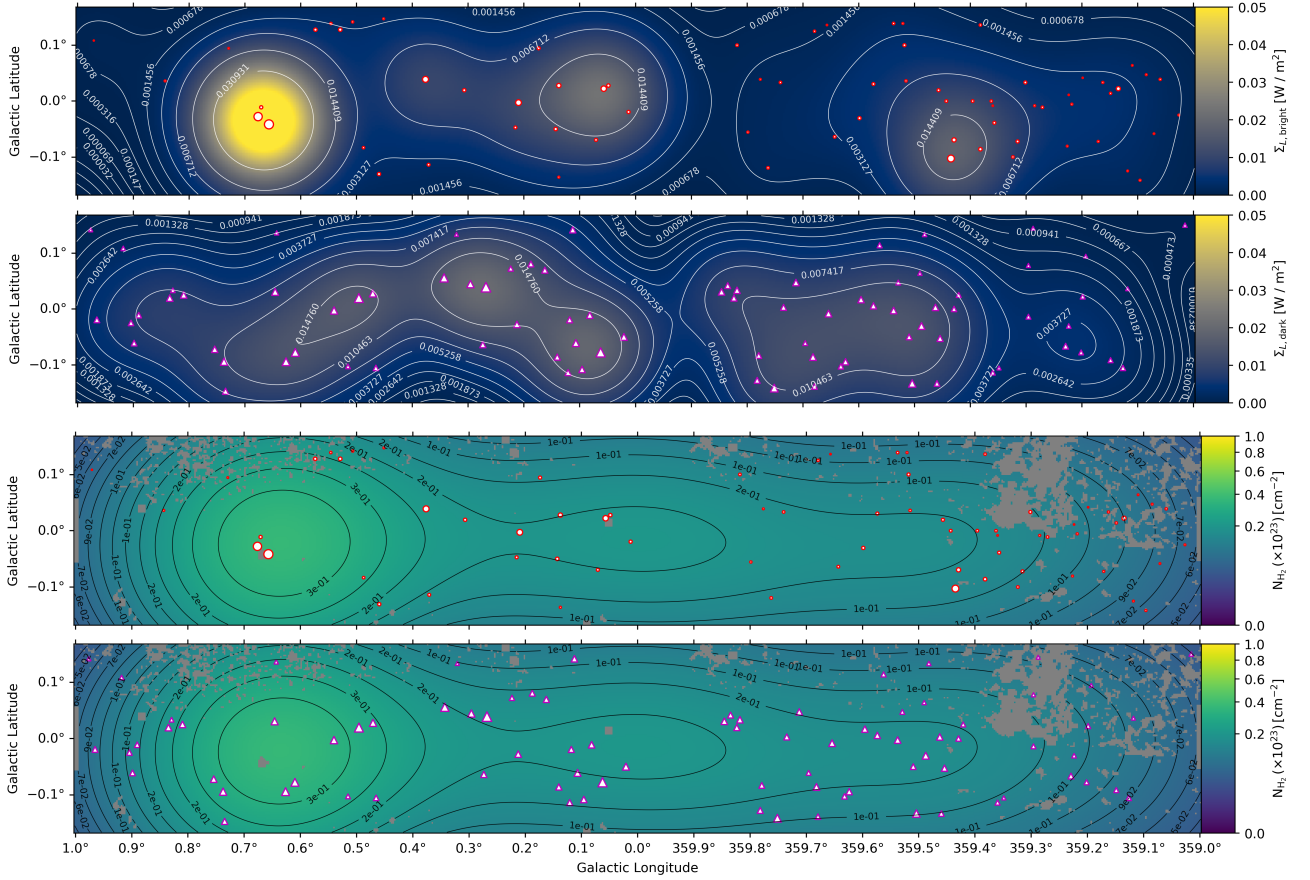


Figure A1. **Top:** The surface luminosity distribution of the 70- μm Hi-GAL sources used to determine the star formation efficiency (SFE) in Fig. 10. **Second:** The surface luminosity distribution for the 160–500- μm sources. Each marker size is proportional to the square root of the source’s total flux. Contours represent the surface luminosity, ranging from the minimum to maximum observed values, with labels indicating specific luminosity levels. **Third:** The H_2 column-density distribution smoothed to 8 arcmins. Each marker shows the position of 70- μm Hi-GAL sources as per the top panel. **Bottom:** As for third top but showing the 160–500- μm sources.